Diagnosis of Eccentric Rotor in Synchronous Machines by Analysis of Split-Phase Currents—Part I: Theoretical Analysis

Claudio Bruzzese, *Member, IEEE*

***Abstract*—This work shows a method to quantify rotor eccentricities in synchronous machines by exploiting the unbalance caused in the split-phase currents. The paper first develops a machine model comprehensive of eccentricities and parallel circuits in the stator, by using symmetrical components. Then, the model is used for formal calculation of the unbalanced currents. Finally, the equations are reversed to obtain eccentricity degrees from current measurements. Practical formulas are given for fault assessment, only requiring machine line voltage and synchronous reactance. The method can be applied on load. This paper provides full details of the theory underlying the method. The theory also clarifies some aspects about split-phase currents, not deepened before. It is proven that the air gap flux modulation due to eccentricities, acting through additional $2(p \pm 1)$-pole flux waves in $2p$-pole machines, stimulates additional currents, which circulate in the stator and turn into $2(p \pm 1)$-pole rotating space vectors in the complex domain. Vector trajectories have shape and amplitude dictated by eccentricity type and degree, respectively. This study is limited to $2p$-pole machines with $p \geq 2$. The theory is corroborated by simulations of a practical 1950-kVA generator in this paper. Experimental proofs and simulations of a laboratory 17-kVA machine are provided in a sequel of this paper.**

***Index Terms*—Condition monitoring, current measurement, eccentricity, fault diagnosis, rotor, space vectors, spectral analysis, synchronous machine (SM).**

NOMENCLATURE

B_0	Maximum flux density in the healthy machine.
D_1, D_2	Amplitudes of $(f \pm f/p)$-frequency signatures of dynamic rotor eccentricity (DRE).
$\boldsymbol{e}$	Column vector of voltages induced by the rotor field.
$\boldsymbol{e}'$	Column vector of transformed induced voltages.
$\vec{e}^{(q)}$	Complex qth sequence voltage induced by the rotor.
$\vec{e}^{(q)}_{(\omega)}$	$2q$-pole $\omega/2\pi$-frequency induced voltage space vector.
f	Fundamental frequency $(= \omega/2\pi)$.
f_r	Rotor rotation mechanical frequency $(= f/p)$.
$\boldsymbol{F}_n$	Fortescue's $n \times n$ generalized transformation matrix.
g_0	Effective air gap length in the healthy machine.
$\boldsymbol{I}_k$	Identity $k \times k$ matrix.
k	Preferred index for circuit numbering $(k = 1, 2, \ldots, n)$.
K_p	Winding factor for the $2p$-pole flux density wave.
$K_{p\pm1}$	Winding factors for $2(p \pm 1)$-pole flux density waves.
l_e	Machine iron stack effective length.
$\boldsymbol{L}_{SS,h}$	Stator inductance matrix for the healthy machine.
$L_{k\delta}$	Mutual inductance of pole-phase groups (PPGs) displaced of the angle $k\delta$.
$L^{(q)}$	qth sequence inductance
M_0	Air gap magnetomotive force (MMF) amplitude.
n	Number of elementary stator PPGs $(= 6p)$.
N_{PPG}	Number of turns of a single PPG.
p	Machine pole pairs.
P_0	Air gap specific permeance in the healthy machine.
q	Preferred index for sequence orders $(q = 0, 1, \ldots, n-1)$.
$\boldsymbol{Q}$	Connection $n \times 3$ matrix.
$\boldsymbol{R}_{SS}$, $\boldsymbol{L}_{SS}$	Stator resistance and inductance $n \times n$ matrices.
$\boldsymbol{R}'_{SS}$, L'_{SS}	Transformed resistance and inductance $n \times n$ matrices.
R_S	Resistance of a stator PPG.
S_1, S_2	Amplitudes of fundamental-frequency signatures of static rotor eccentricity (SRE).
v_X, i_X	Machine phase voltage and current $(X{=}A, B, C)$.
$\boldsymbol{v}_S$, $\boldsymbol{i}_S$	Real stator voltage and current column vectors.
$\boldsymbol{v}'_S$, $\boldsymbol{i}'_S$	Transformed stator voltage and current column vectors.
v_k, i_k	Voltage and current of the kth PPG.
$\vec{v}^{(q)}$, $\vec{i}^{(q)}$	Complex qth sequence stator voltage and current.
v_0, i_0	Three-phase homopolar voltage and current.
$\vec{v}^{s}_{dq}$, $\vec{i}^{s}_{dq}$	Voltage and current Park's space vectors.
V_{LL}	Line–line root mean square (RMS) voltage at the machine terminals.
$\boldsymbol{w}$, $\boldsymbol{\mu}$	Reordered phase voltage and current column vectors.
X_S	Synchronous reactance.
α	Complex unit vector $(= e^{j\delta})$.

Manuscript received May 7, 2012; revised June 28, 2013 and August 14, 2013; accepted August 18, 2013. Date of publication October 1, 2013; date of current version February 7, 2014. This work was supported in part by the Italian Ministry of Defense, General Direction of Navy Armaments, under Contract 19711, December 19, 2007.

The author is with the Department of Astronautical, Electrical, and Energy Engineering, University of Rome "La Sapienza," 00184 Rome, Italy (e-mail: claudio.bruzzese@uniroma1.it).

Color versions of one or more of the figures in this paper are available online at http://ieeexplore.ieee.org.

Digital Object Identifier 10.1109/TIE.2013.2284141

δ	Angular displacement of consecutive PPGs ($= 2\pi/n$).
ΔB	Increment of air gap flux density due to eccentricity.
$\boldsymbol{\Delta L}_{SS}$	Incremental inductance matrix for faulty machine.
$\Delta L^{(q,u)}$	Coupling inductance between sequence circuits q, u.
$\boldsymbol{\Delta\psi}'_{SS}$	Column vector of additional sequence flux linkages.
$\Delta\vec{\psi}_{SS}^{(p\pm1)}$	Additional flux linkages of the sequence circuits $p \pm 1$.
$\Delta\Psi$	Generic flux increment due to eccentricity.
ζ	Air gap field angle on the direct axis (load angle).
θ	Rotor rotation mechanical angle ($= \omega t/p$).
θ_S, θ_R	Angular abscissas in stator and rotor frames.
ρ_s, ρ_d	Static and dynamic per unit eccentricities, $0 \leq \rho_s + \rho_d < 1$.
ξ_s, ξ_d	Angles of static and dynamic eccentricities.
$\boldsymbol{\psi}_{SR}$	Real stator exciting flux linkage column vector.
$\boldsymbol{\psi}'_{SR}$	Transformed stator exciting flux linkage column vector.
ψ_k	Flux linkage of the kth PPG.
$\vec{\psi}_{(w)}^{(q)}$	$2q$-pole $\omega/2\pi$-frequency flux linkage space vector.
Ψ_0	Max PPG flux linkage in the healthy machine.
τ	Stator winding pole pitch.
ω	Fundamental angular frequency ($= 2\pi f$).
$*$	Complex conjugate operator.
$'$	Quantity transformed in the complex domain.

I. Introduction

POWER synchronous machines (SMs) provide vital service for electric energy production and utilization. Machine damages result in costly service interruptions and reparations; thus, SMs are attentively monitored in industry and in power plants [1]. Typical faults in power SMs concern stator and rotor insulation [2]–[5], magnetic cores [1], rotor balance/alignment [6], bearings [7], and other parts (cooling system, slip rings, rotor cage, etc.) [1], [8]. Shaft unbalances and misalignments may produce a stator–rotor rub in the worst case [1], but usually, they cause bearing overheating and abnormal wear due to the unbalanced magnetic pull [6], [9] or even bearing damage due to vibrations and shaft currents [10]. Other major causes of bearing failure are shaft torsional vibrations [11] and defective lubrication [1], [12]. Bearing monitoring is commonly based on vibration [13], [14] and temperature measurements [8] and on analysis of bearing oil [12]. The air gap unbalance monitoring can provide a lot of useful information in addition to bearing monitoring, through the rotor eccentricity (RE) assessment, but the techniques applied on site until now are very invasive and require costly measuring hardware and challenging installation. The air gap was monitored in large generators by using fiber-optic sensors placed on the rotor [15] or by capacitive or inductive probes inside the stator bore [7], [16]. Due to cost reasons, the air gap of small- and/or medium-power SMs is usually simply manually checked, with time-consuming and difficult procedures [9], [12], [17].

Many papers focused on RE detection for condition-based maintenance in induction machines in the last decades [18]–[25]. Phase current monitoring is usually preferred for ease of measurement, although quantitative links between current signatures and eccentricity degree through machine parameters are still under study [18], [20], [21]. The rotor slot passing frequencies stimulated in the phase current of eccentric-rotor motors [19], [25] or the sidebands $f \pm f_r$ around the supply frequency [21], [24] have been exploited. Common problems of these signatures are load dependence [22], [26] and difficulty to distinguish a static RE (SRE) from a dynamic RE (DRE) [23]. As a consequence, indicators of mixed eccentricity overall level were also tried [21], [23]. Separate detection of SRE and DRE by using terminal voltage analysis at machine switch-off is reported in [19]. In addition, the external flux has been used, as in [27], where a DRE-related slip-frequency signature is detected by an axial coil. Although some diagnosis methods investigated for induction machines could be adapted to other revolving-field machines with a rotor cage [24], the zero-slip condition and eventual salient structures [28] require specialized approaches for SM monitoring. Recently investigated techniques for online noninvasive detection of REs in wound-rotor, reluctance and permanent magnet SMs use signatures in the phase current [29] and voltage [30], [31], as well as in the field current [31], [32]. Other invasive methods based on search coils inserted in the machine air gap, for direct air gap flux density sensing, are still investigated nowadays [33]. A more complete review and discussion of these techniques is remanded to [34], for the sake of brevity.

Here, the recently proposed split-phase current signature analysis (SPCSA) technique [9], [12], [35], [36] is better described, which is based on the online measurement and analysis of split-phase currents in armature windings endowed with parallel-connected pole-phase groups (PPGs, i.e., groups of series-connected coils of a phase under a single pole [9]).

The SPCSA technique exploits the flux density amplitude modulation incurring in the air gap of eccentric-rotor SMs and resulting in additional flux density distributions with $2(p \pm 1)$ poles in $2p$-pole machines [35]. The voltages directly induced by these flux distributions cannot produce any component in the phase currents due to the mismatch of pole pairs with the stator winding; their effect is appreciable in the external currents only due to the rotor cage (if present), whose reaction field makes rise $f \pm f_r$ frequencies in the line current, and only in case of mixed RE [21]. This paper contributes in showing that the aforementioned $2(p \pm 1)$-pole flux distributions also stimulate internal $2(p \pm 1)$-pole short-circuit current distributions in a stator with parallel-connected PPGs. These currents can be usefully reverted to complex space vectors through a generalized Fortescue's transformation [35], [37]. The obtained vectors trace epitrochoidal trajectories on the respective complex planes, with amplitudes proportional to the eccentricity, and permit an easy and direct eccentricity fault severity evaluation.

This paper carries out closed-form formulas for practical RE assessment in Section II, which are the basis of the SPCSA, by using symmetrical component analysis. The closed-form formulas allow separate online computation of SRE and DRE, on the basis of the spectral fast Fourier transform (FFT) analysis of

the epitrochoidal space vectors. Only the machine synchronous reactance is needed to apply the formulas, in addition to the line voltage and the pole pair number.

The theory was tested in Section III by simulations carried out by using a coupled-circuit linear model of a six-pole 1950-kVA round-rotor SM (RRSM) with rotor cage and parallel PPGs [35]. The model inductances were computed through a winding function approach (WFA) [17].

The RE indicators proposed in this paper are theoretically independent from the load in unsaturated SMs, but the experiments showed a definite influence of both saturation and load variation. The diagnosis is maximally reliable in no-load reduced voltage conditions.

Reference [34] reports experiments performed on a four-pole 17-kVA SM with controlled artificial eccentricity. Online monitoring through SPCSA is demonstrated by using a virtual instrument linked to a data acquisition board. Moreover, the experiments were matched with nonlinear time-stepping finite-elements simulations, which help to clarify the effect of saturation and load on the performances of the proposed indicators in a real machine.

It is finally remarked that this paper originally applies a particular combination of symmetrical component analysis and FFT analysis to a machine with parallel connections in the stator, for RE diagnosis purposes. However, symmetrical components combined with FFT were also used previously for detection of interturn short circuits [38]. Reference [38] carried out the fault-related inverse sequence impedance starting from phase voltages and currents, passing through the calculation of p-order space vectors for a $2p$-pole machine, and then applying FFT. In addition, parallel connections in the stator were rarely considered in the literature devoted to fault diagnosis [39], [40]. A circuit-oriented induction machine model was carried out in [39] on a conductor-by-conductor basis, suitable for parallel-connected winding modeling. The model was used for stator interturn short circuit and broken bar analysis. Reference [40] instead used finite elements to study the split-phase currents in case of eccentric rotor; however, no explicit formulas were carried out for diagnosis in that paper.

II. Theoretical Analysis

A. Restrictions

The three-phase windings of power SMs are broadly classified as concentric, lap, or wave windings [1]. Wave windings are not considered in the following. Concentric and lap types are characterized by the presence of coils. A number of consecutive or concentric coils are generally series connected to form a PPG, and more PPGs can be customarily series or parallel connected to make up a whole phase, based on machine voltage and current requirements. Only parallel-connected PPGs are considered in the following. Whole-coiled windings have $2p$ PPGs in each phase, whereas half-coiled windings only have p; only the first type is covered here. Moreover, the $n = 6p$ PPGs, which make up the three-phase armature, must be identical and symmetrically distributed, as schematically shown in Fig. 1. An example of a practical winding for a 17-kVA SM is shown in [34, Appendix]. Finally, the study is restricted to round-rotor structures with $p \geq 2$.

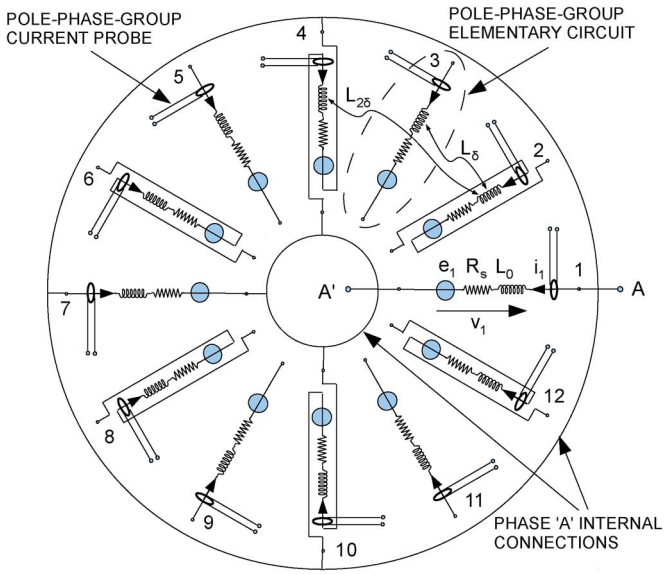

Fig. 1. Four-pole three-phase winding with parallel-connected PPGs.

The $n = 6p$ stator PPGs can be modeled as unconnected mutually coupled circuits with independent currents as follows:

$$\boldsymbol{v}_S = \boldsymbol{R}_{SS}\boldsymbol{i}_S + \frac{d}{dt}(\boldsymbol{L}_{SS}\boldsymbol{i}_S) + \boldsymbol{e}. \tag{1}$$

In (1), $\boldsymbol{i}_S = (i_1, i_2, \ldots, i_n)^t$ represents the stator internal currents, $\boldsymbol{v}_S = (v_1, v_2, \ldots, v_n)^t$ are the PPG voltages, $\boldsymbol{R}_{SS}$ is a diagonal matrix, and $\boldsymbol{L}_{SS}$ contains the stator inductances. The voltages $\boldsymbol{e}$ induced by the rotor are influenced by REs, due to the modulation of the flux density wave traveling in the abnormal air gap. After calculation of the voltages $\boldsymbol{e}$, the internal currents $\boldsymbol{i}_S$ can be carried out from (1) through model transformation and circuit connection. In the following analysis, a no-load machine is first considered (this restriction will be removed later).

B. RRSM Model Transformation

Transformations based on symmetrical components have been usefully applied in the past to polyphase machines for fault analysis [37], [41]. The basic generalized current space transformation is carried out through a $n \times n$ Fortescue's matrix $\boldsymbol{F}_n^*$ with elements $f_{xy} = \alpha^{(x-1)(y-1)}/\sqrt{n}$, where $\alpha = e^{j2\pi/n}$ [37] as follows:

$$\begin{pmatrix} \vec{i}^{(0)} \\ \vec{i}^{(1)} \\ \vec{i}^{(2)} \\ \vdots \\ \vec{i}^{(n-1)} \end{pmatrix} = \frac{1}{\sqrt{n}} \begin{pmatrix} 1 & 1 & 1 & \cdots & 1 \\ 1 & \alpha & \alpha^2 & \cdots & \alpha^{(n-1)} \\ 1 & \alpha^2 & \alpha^4 & \cdots & \alpha^{2(n-1)} \\ & & & \vdots & \\ 1 & \alpha^{(n-1)} & \alpha^{2(n-1)} & \cdots & \alpha^{(n-1)^2} \end{pmatrix} \cdot \begin{pmatrix} i_1 \\ i_2 \\ i_3 \\ \vdots \\ i_n \end{pmatrix}. \tag{2}$$

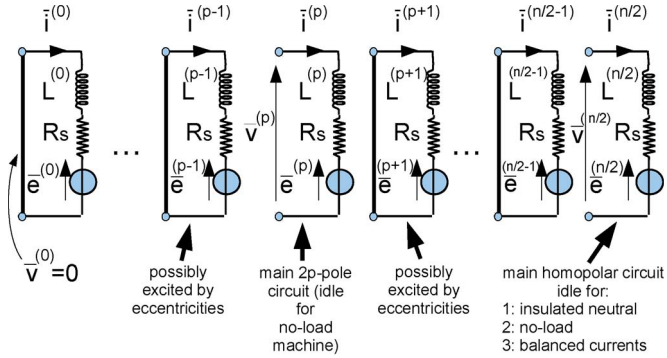

Fig. 2. Stator space-sequence circuits.

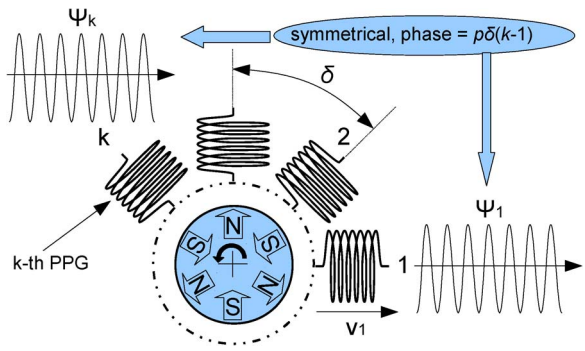

Fig. 3. Centered-rotor machine.

In (2), the complex terms $\vec{i}^{(q)}$ are space-sequence currents (also termed current space vectors). The RRSM stator model (1) is transformed in case of a centered (healthy) rotor machine, i.e., with $\boldsymbol{L}_{SS} = \boldsymbol{L}_{SS,h}$, which is constant and circulant (any row is obtained from the precedent by a circular right shift; thus, only the first row is shown; see Fig. 1 for symbols) as follows:

$$\text{first row of } \boldsymbol{L}_{SS,h} = \\ (\, L_0 \quad L_\delta \quad L_{2\delta} \quad \cdots \quad L_{(n/2)\delta} \quad \cdots \quad L_{2\delta} \quad L_\delta \,). \quad (3)$$

The transformation of (1) leaves unchanged $\boldsymbol{R}_{SS}$ and reverts $\boldsymbol{L}_{SS,h}$ in a diagonal constant real matrix (see Appendix A), thus obtaining the n decoupled space-sequence circuits, as shown in Fig. 2, i.e.,

$$\vec{v}^{(q)} = R_S\, \vec{i}^{(q)} + L^{(q)} \frac{d\, \vec{i}^{(q)}}{dt} + \vec{e}^{(q)},\ q = 0, \ldots, n-1. \quad (4)$$

The qth circuit in (4) is complex conjugate of the $(n-q)$th one; thus, the latter is redundant. The pth circuit is responsible for the main electromechanical energy conversion, and $L^{(p)}$ is related to X_S through $L^{(p)} = pX_S/\pi f$. The $(p \pm 1)$th circuits are sensitive to eventual $2(p \pm 1)$-pole air gap flux density waves. The following steps calculate the sequence voltages $\vec{e}^{(q)}$ in (4), for both healthy and eccentric rotor cases.

Note finally that $\boldsymbol{L}_{SS}$ [which defines the armature reaction in (1)] is influenced by the REs due to a first-order space harmonic in the air gap distribution. The additional first harmonic in $\boldsymbol{L}_{SS}$ can be neglected in no-load conditions (see Appendix B).

C. Machine With Centered Rotor

For the healthy machine, and neglecting higher order space harmonics, the air gap permeance function of the RRSM can be assumed constant: $P = P_0 = \mu_0/g_0$. Moreover, the air gap MMF wave is entirely due to the rotor excitation in the unloaded machine and is written in the rotor frame as

$$M = M_0 \cos\ p\, \theta_R. \quad (5)$$

The MMF wave (5) rotates in the stator frame due to the coordinate change $\theta_R = \theta_S - \omega t/p$. The resulting flux density rotating wave, from $B = PM$, is

$$B = B_0 \cos(\omega t - p\, \theta_S) \quad (6)$$

where $B_0 = P_0 M_0$. The fluxes linked by (6) with the n PPGs make up a single-frequency $2p$-pole symmetric system, as shown in Fig. 3, i.e.,

$$\psi_k = \Psi_0 \cos\left(\omega t - p\delta(k-1)\right),\ k = 1, \ldots, n \quad (7)$$

where Ψ_0 is proportional to B_0 in the unsaturated machine, through $\Psi_0 = (2/\pi) K_p \tau l_e N_{\mathrm{PPG}} B_0$ (for the symbols, see the Nomenclature). In case of parallel-connected PPGs, the amplitude Ψ_0 is fixed by the line–line voltage V_{LL} through $\Psi_0 = \sqrt{2} V_{\mathrm{LL}}/\sqrt{3}\omega$.

The fluxes (7) are converted in the complex domain by applying the same transformation as in (2), and two rotating flux space vectors are obtained, which are complex conjugate, i.e.,

$$\boldsymbol{\psi}'_{SR} = \boldsymbol{F}_n^* \boldsymbol{\psi}_{SR} \\ = \left(0 \cdots 0 \quad \vec{\psi}^{(p)}_{(\omega)} \quad 0 \cdots 0 \quad \vec{\psi}^{(n-p)}_{(\omega)} \quad 0 \cdots 0\right)^t. \quad (8)$$

In (8), $\boldsymbol{\psi}_{SR} = (\psi_1, \psi_2, \ldots, \psi_n)^t$ is the column vector of the real PPG flux linkages (7), and $\boldsymbol{\psi}'_{SR}$ contains the correspondent sequence fluxes; the $2p$-pole complex vector $\vec{\psi}^{(p)}_{(\omega)}$ in (8) is

$$\vec{\psi}^{(p)}_{(\omega)} = \frac{\sqrt{n}}{2} \Psi_0 e^{j\omega t}. \quad (9)$$

The correspondent $2p$-pole induced voltage space vector to be put in (4) in case of a centered-rotor machine is

$$\vec{e}^{(p)}_{(\omega)} = \frac{d}{dt} \vec{\psi}^{(p)}_{(\omega)}. \quad (10)$$

D. Case of Static Eccentricity

With rotor center statically displaced, the air gap permeance function is (the symbols are explained in Fig. 4)

$$P(\theta_S) = \frac{\mu_0/g_0}{1 - \rho_s \cos(\theta_S - \xi_s)} \simeq P_0\, (1 + \rho_s \cos(\theta_S - \xi_s)) \quad (11)$$

which combines with the MMF wave (5). The flux density wave turns out as in (12). The amplitude is spatially modulated in proportion to ρ_s, assuming $\Delta B_s = \rho_s B_0$ [21], [35], [42], as shown in Fig. 5, i.e.,

$$B = (B_0 + \Delta B_s \cos(\theta_S - \xi_s)) \cdot \cos(\omega t - p\theta_S). \quad (12)$$

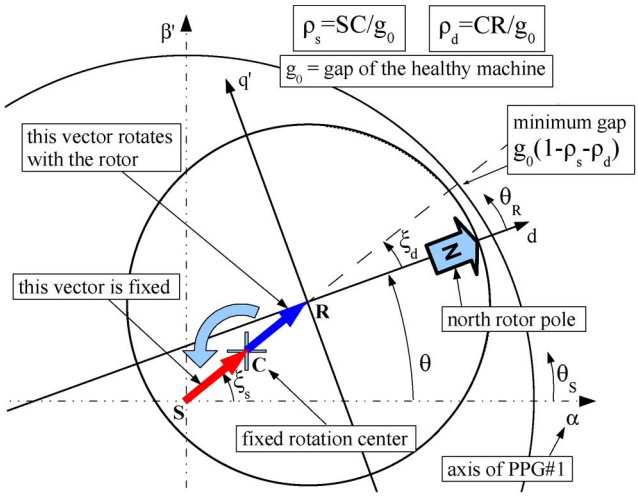

Fig. 4. Rotor eccentricity scheme and symbols used in the formulas.

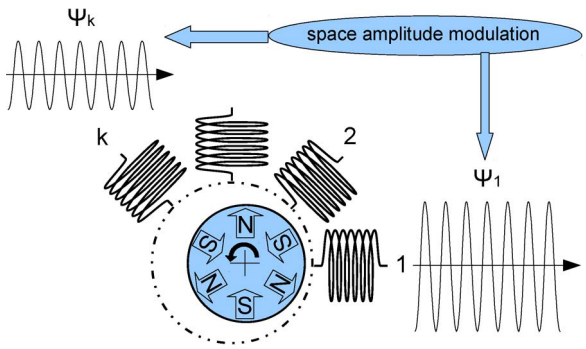

Fig. 5. Case of static eccentricity.

The decomposition of the wave (12) yields two new $2(p\pm1)$-pole waves superimposed to the flux density (6) of the healthy machine. They can be thought as produced by two "virtual" rotors with $2(p\pm1)$ poles and speed $\omega/(p\pm1)$ [9]. The correspondent stator-linked fluxes are readily obtained by integration as

$$\begin{aligned}\psi_k &= \Psi_0\cos\left(\omega t - p\delta(k-1)\right)\\ &+ \Delta\Psi_{s,p-1}\cos\left(\omega t-(p-1)\delta(k-1)-\xi_s\right)\\ &+ \Delta\Psi_{s,p+1}\cos\left(\omega t-(p+1)\delta(k-1)+\xi_s\right)\end{aligned}\quad(13)$$

where the additional flux systems due to SRE have amplitudes

$$\Delta\Psi_{s,p\pm1}=\frac{\rho_s\Psi_0}{2}K_{p\pm1}.\quad(14)$$

The coefficients $K_{p\pm1}$ are subharmonic winding factors (see Appendix C for their calculation).

The transformation of the additional fluxes in (13) produces two fundamental-frequency $2(p\pm1)$-pole rotating space vectors, whose amplitudes are proportional to ρ_s, i.e.,

$$\vec{\psi}^{(p-1)}_{(\omega)}=\frac{\sqrt{n}}{2}\Delta\Psi_{s,p-1}e^{j(\omega t-\xi_S)}\quad(15)$$

$$\vec{\psi}^{(p+1)}_{(\omega)}=\frac{\sqrt{n}}{2}\Delta\Psi_{s,p+1}e^{j(\omega t+\xi_S)}.\quad(16)$$

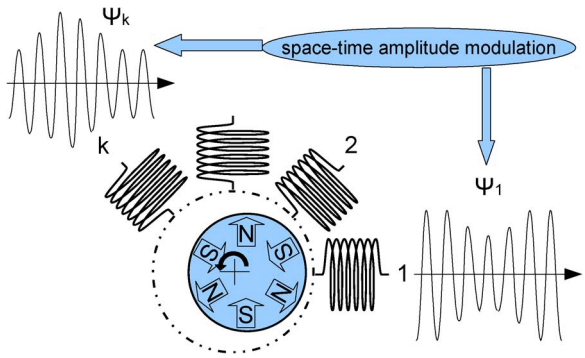

Fig. 6. Case of dynamic eccentricity.

E. Case of Dynamic Eccentricity

With rotor center dynamically displaced, as shown in Fig. 6, the flux density wave amplitude is modulated in both space and time as in (17). The maximum flux variation is $\Delta B_d=\rho_d B_0$, i.e.,

$$B=(B_0+\Delta B_d\cos(\omega t/p-\theta_S+\xi_d))\cdot\cos(\omega t-p\theta_S).\quad(17)$$

The decomposition of (17) again yields two new $2(p\pm1)$-pole waves, but with different frequencies, as produced by two virtual $2(p\pm1)$-pole rotors running with the same speed ω/p [9]. The stator-linked fluxes are carried out as

$$\begin{aligned}\psi_k &= \Psi_0\cos\left(\omega t-p\delta(k-1)\right)\\ &+ \Delta\Psi_{d,p-1}\cos\left((\omega-\omega/p)t-(p-1)\delta(k-1)-\xi_d\right)\\ &+ \Delta\Psi_{d,p+1}\cos\left((\omega+\omega/p)t-(p+1)\delta(k-1)+\xi_d\right)\end{aligned}\quad(18)$$

where

$$\Delta\Psi_{d,p\pm1}=\frac{\rho_d\Psi_0}{2}K_{p\pm1}.\quad(19)$$

The sequence components of the additional fluxes in (18) are as follows:

$$\vec{\psi}^{(p-1)}_{(\omega-\omega/p)}=\frac{\sqrt{n}}{2}\Delta\Psi_{d,p-1}e^{j((\omega-\omega/p)t-\xi_d)}\quad(20)$$

$$\vec{\psi}^{(p+1)}_{(\omega+\omega/p)}=\frac{\sqrt{n}}{2}\Delta\Psi_{d,p+1}e^{j((\omega+\omega/p)t+\xi_d)}.\quad(21)$$

F. Case of Mixed Eccentricity

In the general case of mixed-type fault, the fluxes (13) and (18) coexist. In addition to (10), the following voltages finally appear:

$$\vec{e}^{(p-1)}=\frac{d}{dt}\left(\vec{\psi}^{(p-1)}_{(\omega)}+\vec{\psi}^{(p-1)}_{(\omega-\omega/p)}\right)\quad(22)$$

$$\vec{e}^{(p+1)}=\frac{d}{dt}\left(\vec{\psi}^{(p+1)}_{(\omega)}+\vec{\psi}^{(p+1)}_{(\omega+\omega/p)}\right).\quad(23)$$

The voltages (22) and (23) are not able to induce any component in the machine phase current due to the pole pair mismatch with the $2p$-pole sequence circuit shown in Fig. 2. However, the $(p\pm1)$-order sequence circuits are properly stimulated. The calculation of the $(p\pm1)$-order reaction currents can be

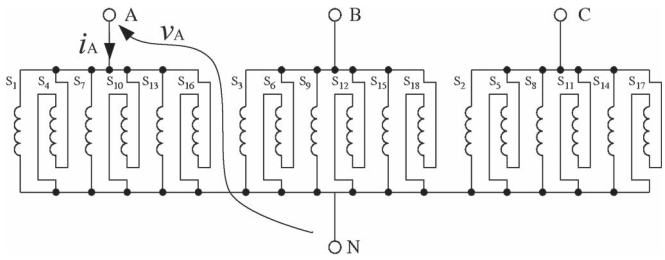

Fig. 7. Stator winding with parallel PPGs (example for $p = 3$, $n = 18$).

performed by using (4), but preliminarily, the electrical constraints (due to the winding internal connections with parallel PPGs) must be transferred to the sequence circuits. In fact, the sequence voltages and currents $\vec{v}^{(q)}$, $\vec{i}^{(q)}$ are not free variables when the actual armature internal connections are taken in account.

G. Connection of the Sequence Circuits

A parallel-connected winding is shown in Fig. 7. This scheme is often used in low-voltage high-current SMs, as onboard ship [17] or wind [5] generators. The electrical constraints (24) and (25) apply to the real voltages and currents of phase A in Fig. 7, i.e.,

$$v_A = v_1 = -v_4 = v_7 = -v_{10} = v_{13} = -v_{16} \tag{24}$$

$$i_A = i_1 - i_4 + i_7 - i_{10} + i_{13} - i_{16}. \tag{25}$$

Similar equations hold for phases B and C. The voltage constraints are synthetically written by using a connection matrix $\boldsymbol{Q}$, i.e.,

$$\boldsymbol{v}_s = \boldsymbol{Q} \cdot \boldsymbol{w} \tag{26}$$

where $\boldsymbol{Q} = [\boldsymbol{I}_3 - \boldsymbol{I}_3 \ \boldsymbol{I}_3 - \boldsymbol{I}_3 \ldots]^t$, and $\boldsymbol{w} = [w_1 \ w_2 \ w_3]^t = [v_A, -v_C, v_B]^t$ is a properly defined voltage vector. $\boldsymbol{I}_3$ is an identity (3×3) matrix.

Equation (26) is put in the first of (A2), thus transferring the constraints on the components of $\boldsymbol{v}'_S$ as follows:

$$\vec{v}^{(q)} = \frac{1}{\sqrt{n}} \sum_{k=0}^{2p-1} (-\alpha^{3q})^k \cdot \sum_{u=1}^{3} \alpha^{(u-1)q} w_u. \tag{27}$$

The sequence voltages are finally obtained from (27) as

$$\vec{v}^{(q)} = \begin{cases} 0 & \text{for } q \neq \pm p, n/2 \\ \frac{2p}{\sqrt{n}}(w_1 + \alpha^q w_2 + \alpha^{2q} w_3) & \text{for } q = \pm p, n/2 \end{cases} \tag{28}$$

which proves that the sequence circuits are all short circuited, except those for $q = \pm p$, $n/2$, as shown in Fig. 2. From (28), the circuits for $q = \pm p$, $n/2$ turn out to be fed by the following complex voltages $\vec{v}^{(n/2)}$, $\vec{v}^{(\pm p)}$:

$$\begin{bmatrix} \vec{v}^{(n/2)} \\ \vec{v}^{(p)} \\ \vec{v}^{(-p)} \end{bmatrix} = \frac{\sqrt{2p}}{\sqrt{3}} \begin{bmatrix} 1 & 1 & 1 \\ 1 & e^{j\,120^\circ} & e^{j\,240^\circ} \\ 1 & e^{-j\,120^\circ} & e^{-j\,240^\circ} \end{bmatrix} \cdot \begin{bmatrix} v_A \\ v_B \\ v_C \end{bmatrix} = \sqrt{2p} \begin{bmatrix} v_0 \\ \vec{v}^{s}_{dq} \\ \vec{v}^{s*}_{dq} \end{bmatrix} \tag{29}$$

and it is easily recognized that they coincide with the classical three-phase homopolar component v_0 (real valued) and Park's complex vectors $\vec{v}^{s}_{dq}$, $\vec{v}^{s*}_{dq}$ written in the stator frame [43].

In a similar way, the current constraints are applied by

$$\boldsymbol{\mu} = \boldsymbol{Q}^t \cdot \boldsymbol{i}_s \tag{30}$$

where $\boldsymbol{\mu} = [\mu_1 \ \mu_2 \ \mu_3]^t = [i_A, -i_C, i_B]^t$. The second of (A2) must be substituted in (30), thus obtaining

$$\mu_u = \sum_{q=0}^{n-1} \vec{i}^{(q)} \frac{1}{\sqrt{n}} \alpha^{-(u-1)q} \cdot \left(\sum_{k=0}^{2p-1} (-\alpha^{3q})^k \right) \tag{31}$$

which can be simplified and posed in explicit form with respect to $\vec{i}^{(n/2)}$, $\vec{i}^{(\pm p)}$ as follows:

$$\begin{bmatrix} \vec{i}^{(n/2)} \\ \vec{i}^{(p)} \\ \vec{i}^{(-p)} \end{bmatrix} = \frac{1}{\sqrt{6p}} \begin{bmatrix} 1 & 1 & 1 \\ 1 & e^{j\,120^\circ} & e^{j\,240^\circ} \\ 1 & e^{-j\,120^\circ} & e^{-j\,240^\circ} \end{bmatrix} \cdot \begin{bmatrix} i_A \\ i_B \\ i_C \end{bmatrix} = \frac{1}{\sqrt{2p}} \begin{bmatrix} i_0 \\ \vec{i}^{s}_{dq} \\ \vec{i}^{s*}_{dq} \end{bmatrix}. \tag{32}$$

The latter proves that only the sequence currents for $q = \pm p$, $n/2$ are constrained, and they coincide with the three-phase current homopolar component i_0 and Park's vectors $\vec{i}^{s}_{dq}$, $\vec{i}^{s*}_{dq}$. This means that, in Fig. 2, the circuits for $q = p$, $n/2$ should be connected to the correspondent sequence circuits of the external network to realize the needed current constraints. All the other circuits are not current constrained, and, being short-circuited, they can be individually solved.

H. Calculation of the $(p \pm 1)$-Order Sequence Currents

When an RE appears, currents arise in the $(p \pm 1)$-order circuits, which can be used for fault diagnosis. By using (4), (14), (15), (19), (20), and (22) and by neglecting the resistance R_S, the steady-state $(p-1)$-order current can be carried out as

$$\vec{i}^{(p-1)} = \frac{-\sqrt{n}\Psi_0/4}{L^{(p-1)}/K_{p-1}} \left[\rho_S e^{j(\omega t - \xi_s)} + \rho_d e^{j((\omega - \omega/p)t - \xi_d)} \right]. \tag{33}$$

A similar solution holds for the $(p+1)$-order circuit, i.e.,

$$\vec{i}^{(p+1)} = \frac{-\sqrt{n}\Psi_0/4}{L^{(p+1)}/K_{p+1}} \left[\rho_s e^{j(\omega t + \xi_s)} + \rho_d e^{j((\omega + \omega/p)t + \xi_d)} \right]. \tag{34}$$

Each of (33) and (34) has two components proportional to SRE and DRE, respectively. These biperiodic currents trace closed epitrochoidal loci on the respective complex planes, as shown in Section III-B. The use of (33) and (34) for fault diagnosis is straightforward, passing through the spectral analysis of the complex currents carried out for a given machine.

However, the parameters $L^{(p\pm1)}$ are hardly furnished in the manufacturer's data sheets, which is an obstacle to the handy use of (33) and (34) for an absolute estimation of REs. A possible solution to this problem is carried out in the next point.

I. Definition of Practical Fault Indicators

The complex currents (33) and (34) are first rewritten in a more practical way as follows:

$$\vec{i}^{(p-1)} = S_1 e^{j(\omega t-\xi_s)} + D_1 e^{j((\omega-\omega/p)t-\xi_d)} \tag{35}$$

$$\vec{i}^{(p+1)} = S_2 e^{j(\omega t+\xi_s)} + D_2 e^{j((\omega+\omega/p)t+\xi_d)}. \tag{36}$$

The symbols S_1, D_1, S_2, and D_2 represent the amplitudes of the frequency components obtained by complex FFT analysis of vectors calculated from the measured currents. One estimation of SRE and one of DRE can be carried out from (35) as follows:

$$\rho_s = \frac{L^{(p-1)}/K_{p-1}}{\sqrt{n}\Psi_0/4} S_1 \tag{37}$$

$$\rho_d = \frac{L^{(p-1)}/K_{p-1}}{\sqrt{n}\Psi_0/4} D_1. \tag{38}$$

Other two estimations are similarly carried out from (36) as follows:

$$\rho_s = \frac{L^{(p+1)}/K_{p+1}}{\sqrt{n}\Psi_0/4} S_2 \tag{39}$$

$$\rho_d = \frac{L^{(p+1)}/K_{p+1}}{\sqrt{n}\Psi_0/4} D_2. \tag{40}$$

Equations (37) and (39) can be now easily combined and averaged to obtain a single more reliable estimation of SRE, by using the following general property (see Appendix D):

$$L^{(p)} \simeq \frac{L^{(p-1)}/K_{p-1} + L^{(p+1)}/K_{p+1}}{2}. \tag{41}$$

The same is done for (38) and (40). By also exploiting $L^{(p)} = 2pX_S/\omega$ and $\psi_0 = \sqrt{2}V_{\rm LL}/\sqrt{3}\omega$, the conclusive formulas for direct SRE and DRE estimation are carried out as

$$\rho_s = \frac{S_1 S_2}{S_1 + S_2} \cdot \frac{8\sqrt{p}X_S}{V_{\rm LL}} \tag{42}$$

$$\rho_d = \frac{D_1 D_2}{D_1 + D_2} \cdot \frac{8\sqrt{p}X_S}{V_{\rm LL}}. \tag{43}$$

Equations (42) and (43) are the basis of the proposed eccentricity diagnosis method in round-rotor machines. The unsaturated synchronous reactance and the actual line–line voltage are used. Apart from using FFT, S_1, D_1, S_2, and D_2 in (42) and (43) can be also obtained by measuring maximum ($A = D + S$: vector alignment) and minimum ($B = D - S$: vector opposition) amplitudes of the trajectories traced by vectors (35) and (36) and solving the system for D and S. This more intuitive approach will be used in Section III-B.

J. Extension of (42) and (43) to the Loaded Operation

As shown in Appendix B, additional voltages $d\,\Delta\vec{\psi}_{SS}^{(p\pm1)}/dt$ are induced in the $(p \pm 1)$ circuits in Fig. 2 in loaded conditions due to the load current $\vec{i}^{(p)}$ [see (B6)]. The effect of these additional voltages is qualitatively discussed here, for completeness. Under the combined effect of both rotor excitation and armature reaction in the loaded operation, the air gap MMF (5) changes as

$$M = M_0 \cos(p\theta_R + \zeta) \tag{44}$$

where a load angle ζ appears (the axis of the total MMF wave deviates from the rotor direct axis, lagging for generator operation). The load angle ζ is zero in no-load condition, or for pure reactive load. The total air gap flux density wave also lags of the same angle in the RRSM, i.e.,

$$B = B_0 \cos(\omega t - p\theta_S - \zeta) \tag{45}$$

where $B_0 = P_0 M_0$ always. Finally, the total fluxes linked by (45) with the n PPGs report the same lag, i.e.,

$$\psi_k = \Psi_0 \cos(\omega t - p\delta(k-1) - \zeta),\ k = 1, \ldots, n \tag{46}$$

where $\Psi_0 = (2/\pi)K_p \tau l_e N_{\rm PPG} B_0$. Note that, with a regulated line–line voltage $V_{\rm LL}$, the total flux linkage amplitude Ψ_0 is always fixed by $\Psi_0 = \sqrt{2}V_{\rm LL}/\sqrt{3}\omega$ as in the no-load condition. Thus, the flux density wave (45) has the same amplitude as in the no-load condition, and only the angular displacement ζ distinguishes the loaded from the no-loaded operation in the air gap. In case of eccentricity, the wave (45) is amplitude modulated exactly as in the no-load condition, and a lag finally appears in the voltages induced in the $p \pm 1$ circuits in Fig. 2, i.e.,

$$\left(\frac{d}{dt}\Delta\vec{\psi}_{SS}^{(p\pm1)} + \vec{e}_{load}^{(p\pm1)}\right) = \vec{e}_{no-load}^{(p\pm1)} \cdot e^{-j\zeta}. \tag{47}$$

The circuits in Fig. 2 can be so used (decoupled) in loaded operation, too, by only taking in account the lagging angle ζ. The currents (35) and (36), consequently, simply change as follows:

$$\vec{i}^{(p-1)} = \left(S_1 e^{j(\omega t-\xi_s)} + D_1 e^{j((\omega-\omega/p)t-\xi_d)}\right) \cdot e^{-j\zeta} \tag{48}$$

$$\vec{i}^{(p+1)} = \left(S_2 e^{j(\omega t+\xi_s)} + D_2 e^{j((\omega+\omega/p)t+\xi_d)}\right) \cdot e^{-j\zeta} \tag{49}$$

and the diagnostic formulas (42) and (43) maintain their (theoretical) validity under loaded machine operation, too.

A proof of this fact is shown in the following simulations.

III. Simulations Through WFA

A. Internal Current Waveforms

Simulations were carried out for a six-pole 1950-kVA RRSM at rated voltage and speed (machine data are in Appendix E). The machine has six parallel PPGs per phase. A WFA-based model was used (details are in [17] and [35], and they are not repeated here). The no-load simulations in Figs. 8–11 show the

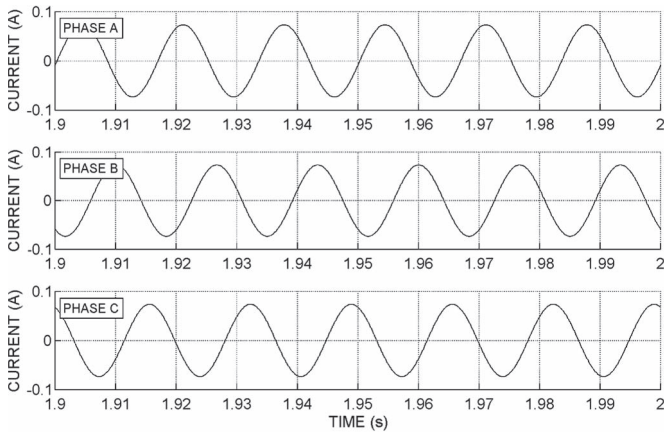

Fig. 8. Stator internal currents, no load, healthy machine (1950-kVA RRSM).

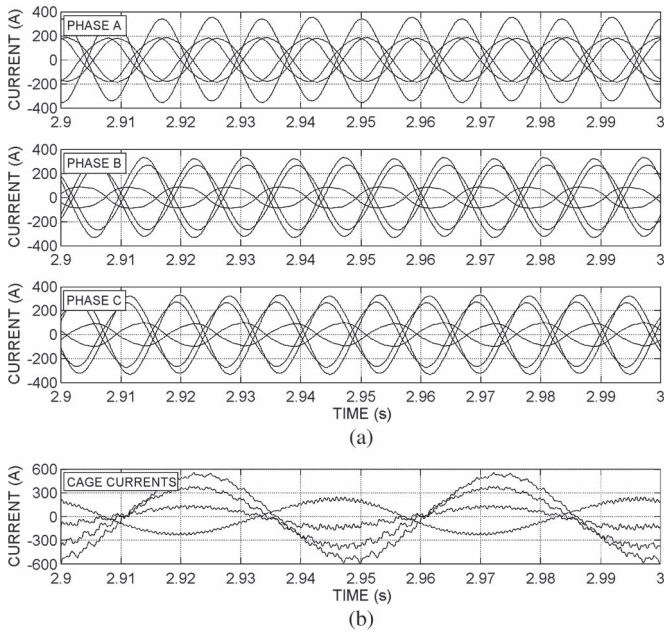

Fig. 9. Case of 66% SRE, no load (1950-kVA RRSM). (a) Stator internal currents. (b) Cage loop currents on a half-pole.

effect of REs on the internal currents, without superimposition of load currents. High load impedances simulate the open circuit; thus, the currents in Fig. 8 are not zero, and the current equilibrium in the healthy SM can be appreciated (six currents per phase are displayed, in which three are reversed; thus, they are all superimposed). With 66% of SRE, large internal currents arise, as shown in Fig. 9(a), which are comparable with the rated current (note that the PPG's current rating is $2502\ \mathrm{A}/6 = 417\ \mathrm{A}$). The current amplitudes depend on coil position, and a space amplitude modulation occurs. Large cage currents also arise, as shown in Fig. 9(b), with rotor-rotation frequency. They produce a counter-rotating field fixed in the stator frame, which dampens the field modulation due to SRE. A 66% of DRE stimulates currents [see Fig. 10(a)] with identical delayed waveforms and with amplitudes analogous to those in Fig. 9(a). No cage current appears, as shown in Fig. 10(b). Finally, Fig. 11(a) shows a case of mixed RE. Since SRE and DRE are equal, the rotor moves from a centered position to a fully

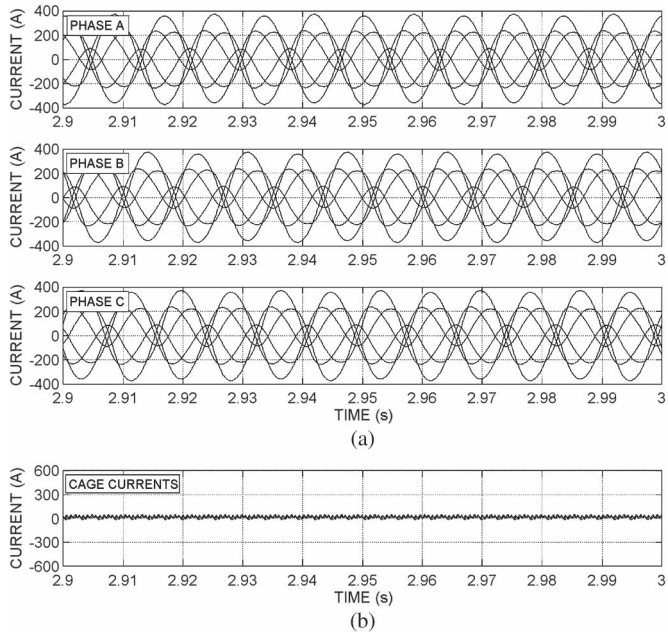

Fig. 10. Case of 66% DRE, no load (1950-kVA RRSM). (a) Stator internal currents. (b) Cage loop currents on a half-pole.

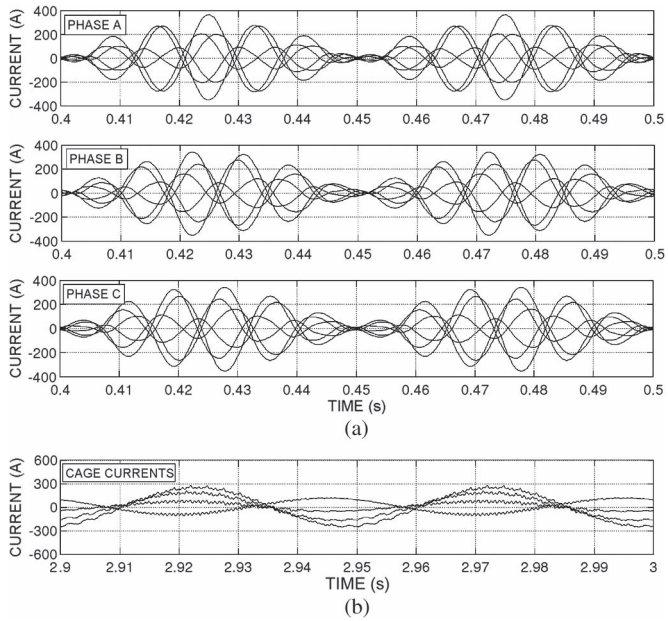

Fig. 11. Case of 33% SRE + 33% DRE, no load (1950-kVA RRSM). (a) Stator internal currents. (b) Cage loop currents on a half-pole.

displaced one in a half-round, and the currents are modulated accordingly. The cage currents in Fig. 11(b) are roughly halved with respect to Fig. 9(b). The stator currents in Figs. 9–11 clearly denounce a faulty condition, but their evaluation is not simple. The space vector analysis in the next point gives a much more clear picture.

B. Analysis Through Space Vectors

By applying the transformation (2), $n/2+1$ time-varying space vectors are obtained [35] starting from the simulated stator currents (the last $n/2-1$ vectors in (2) are redundant).

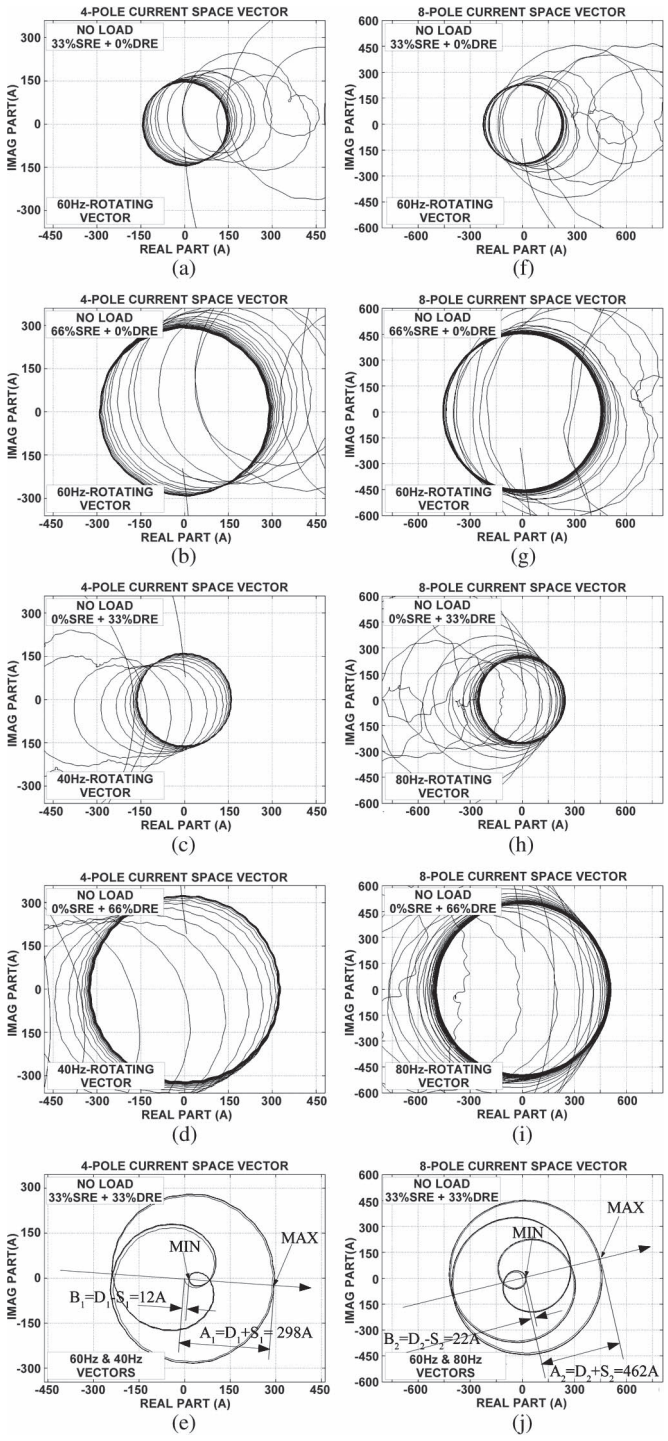

Fig. 12. (a)–(j) $2(p \pm 1)$-pole current space vectors, no-load 1950-kVA RRSM.

Fig. 12 shows the effect of various REs on the $(p \pm 1)$-order vectors, for 33% and 66% of SRE and DRE, and for mixed-type fault, in the no-load 1950-kVA RRSM. All the $n/2 + 1$ vectors react to the RE fault (apart from the six-pole vector, which remains zero in no-load conditions), but only the $(p \pm 1)$-order vectors assume very large amplitudes. The vector amplitudes in Fig. 12 proportionally increase with the RE gravity, and epitrochoidal trajectories appear in case of mixed-type fault, as theoretically previewed by (33) and (34).

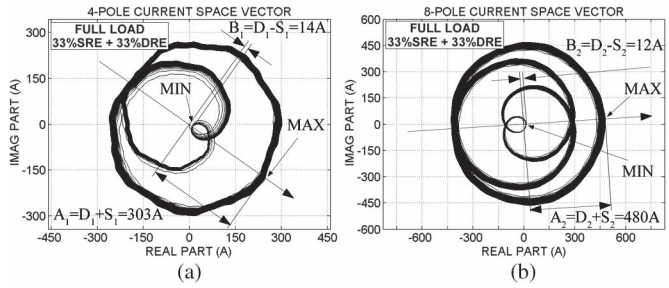

Fig. 13. (a) and (b) $2(p \pm 1)$-pole current space vectors, full-load 1950-kVA RRSM.

Note that, e.g., the $(p-1)$-order vector (four-pole vector for the machine with $p = 3$) in Fig. 12(e) is made up of two rotating components at 60 and 40 Hz, which align themselves every three rounds of the 60-Hz component or two rounds of the 40-Hz component. The epitrochoidal loci have maximum amplitudes proportional to the total fault (static + dynamic), and moreover, they pass close to the axis origin, when the two rotating current components with equal amplitudes are opposed. For the healthy machine, these loci become negligibly small (no figure has been shown for this trivial case). By applying (42) and (43), using the parameters in Appendix E, good estimations of REs can be evaluated back from Fig. 12(e)–(j), (i.e., $\rho_s = 28.8\%$, $\rho_d = 31.4\%$), thus proving the effectiveness of the proposed method when applied to a linear model. The cage reaction lightly dampens the SRE-related indicator, as expected. Finally, Fig. 13 shows a simulation at full load.

A load current appears in the pth circuit in Fig. 2; however, the $(p \pm 1)$-order vector amplitudes in Fig. 13 are quite unaffected in the regulated-voltage machine [compare with Fig. 12(e) and (j)]. The stator reaction only modifies the load angle, and thus, the vectors (48) and (49) appear lagging in Fig. 13 with respect to the positive rotation sense (the actual lag angle is different for the two vectors due to the action of the cage; it is the same when the cage in the simulations is suppressed).

Equations (42) and (43) still give satisfying diagnosis on load ($\rho_s = 29.7\%$, $\rho_d = 32\%$). However, experiments showed deviations from the linear theory in the saturated loaded 17-kVA machine studied in [34]. The reader will find in [34] a practical implementation of (42) and (43) with a discussion of effects due to the saturation incurring in the real machine.

IV. Conclusion

In this paper, a new SPCSA-based method [9], [35] for eccentricity monitoring in SMs with parallel PPGs and $p \geq 2$ has been theoretically detailed. Analytical formulations of split-phase currents through symmetrical components are provided, and practical formulas for RE diagnosis are carried out. WFA-based simulations of a faulty 1950-kVA generator confirm the theory, showing good diagnosis performances of the method. Stator windings with mixed series/parallel connections or $p = 1$ can be studied following the theoretical guidelines furnished in this paper. Method extension to salient-pole structures or to other kinds of revolving-field machines can be also attempted and will be object of future work.

Reference [34] shows controlled tests performed on a laboratory 17-kVA machine, by using a regulated eccentric flange and a virtual instrument. Method performances have been evaluated for various voltage and load levels. Good quantitative RE assessment is reported in case of reduced voltage no-load operation (unsaturated operation). Assessment worsening for full voltage loaded operation has been reported and explained through comparative linear and nonlinear time-stepping finite-element simulations of the 17-kVA machine.

The SPCSA technique has been first developed for online automated condition monitoring of generators on board Italian Navy's ships [12]. A practical 1950-kVA onboard generator is targeted for further research [9]. However, applications to split-phase turbogenerators (often equipped with split-phase current probes for differential protection against winding faults [1]) are conceivable. Among other possible applications, wind generators (with gearboxes or even direct-driven plants) are targeted since they are heavily mechanically solicited, and major firms now call for effective fault diagnosis tools and condition-based maintenance [5].

APPENDIX A
RRSM STATOR MODEL TRANSFORMATION

The stator model (1) is transformed as follows:

$$\boldsymbol{v}'_S = \boldsymbol{R}'_{SS}\boldsymbol{i}'_S + \boldsymbol{L}'_{SS,h}\frac{d\boldsymbol{i}'_S}{dt} + \boldsymbol{e}' \tag{A1}$$

where the transformed quantities are

$$\boldsymbol{v}'_S = \boldsymbol{F}_n^*\boldsymbol{v}_S,\ \boldsymbol{i}'_S = \boldsymbol{F}_n^*\boldsymbol{i}_S,\ \boldsymbol{e}' = \boldsymbol{F}_n^*\boldsymbol{e} \tag{A2}$$

$$\boldsymbol{R}'_{SS} = \boldsymbol{F}_n^*\boldsymbol{R}_{SS}\boldsymbol{F}_n = \boldsymbol{R}_{SS} = diag\{R_S\} \tag{A3}$$

$$\boldsymbol{L}'_{SS,h} = \boldsymbol{F}_n^*\boldsymbol{L}_{SS,h}\boldsymbol{F}_n = diag\{L^{(q)}\}. \tag{A4}$$

The sequence inductances in (A4) are defined as

$$L^{(q)} = L^{(n-q)} = \sum_{u=0}^{n-1} L_{u\delta}\cos(qu\delta). \tag{A5}$$

APPENDIX B
EFFECT OF ECCENTRICITIES ON THE STATOR INDUCTANCE MATRIX

A DRE makes the elements of $\boldsymbol{L}_{SS}$ in (1) fluctuate during the rotor rotation in the RRSM. An SRE, on the other hand, only produces a steady change in the inductance values. The two effects are superimposed in case of mixed-type fault, as shown in Fig. 14. Since SRE and DRE degrees are equal in Fig. 14, the rotor will be centered in a given position (at 0°) and fully eccentric after a half-rotation (see also the scheme in Fig. 4 for $\xi_s = 0$, $\xi_d = \pi$). Thus, the inductance values at 0° are those of the healthy machine ($\boldsymbol{L}_{SS,h}$). Under the combined effect of SRE and DRE, $\boldsymbol{L}_{SS}$ is no longer constant and circulant [compare Fig. 15(a) and (b)].

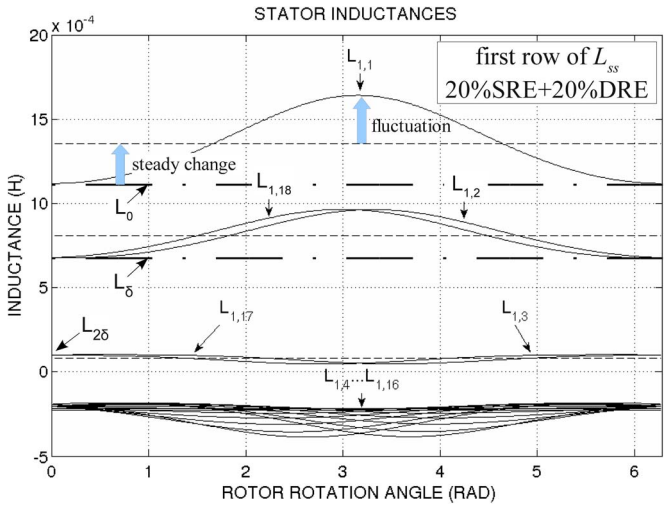

Fig. 14. Stator inductances of a 1950-kVA six-pole RRSM with eccentricity.

In Fig. 15(b), $\Delta\boldsymbol{L}_{SS}$ regroups both steady changes and fluctuations over $\boldsymbol{L}_{SS,h}$ due to rotor misalignment. Thus

$$\boldsymbol{L}_{SS} = \boldsymbol{L}_{SS,h} + \boldsymbol{\Delta L}_{SS}. \tag{B1}$$

Due to $\Delta\boldsymbol{L}_{SS}$ in (B1), the transformation of $\boldsymbol{L}_{SS}$ by (A4) yields a matrix $\boldsymbol{L}'_{SS}$, which is no longer a constant, real, and diagonal matrix. Fig. 16(a) and (b) shows that complex nondiagonal elements appear in $\boldsymbol{L}'_{SS}$. This means that the circuits in Fig. 2 are coupled in the eccentric-rotor machine (i.e., the sequence currents are not independent). However, the diagonal real elements in Fig. 16(a) do not noticeably change with respect to those of the centered-rotor machine, as shown in Fig. 17, for the heavy 40% of the total RE considered. Hence, only the coupling due to the nondiagonal elements in Fig. 16(a) is of concern here. The structure of the matrix $\boldsymbol{L}'_{SS} = \boldsymbol{L}'_{SS,h} + \Delta\boldsymbol{L}'_{SS}$ is as presented in (B2), shown at the bottom of the page, where the diagonal elements belong to $\boldsymbol{L}'_{SS,h}$ and the subdiagonal elements to $\Delta\boldsymbol{L}'_{SS}$. By putting (B1) in (1) and by applying the space transformation, we obtain, in place of (A1), the following:

$$\boldsymbol{v}'_S = \boldsymbol{R}'_{SS}\boldsymbol{i}'_S + \boldsymbol{L}'_{SS,h}\frac{d}{dt}\boldsymbol{i}'_S + \frac{d}{dt}\boldsymbol{\Delta\psi}'_{SS} + \boldsymbol{e}' \tag{B3}$$

$$\boldsymbol{L}'_{SS} = \begin{pmatrix} \ddots & & & & & & \\ & \Delta L^{(p-1,p-2)} & L^{(p-1)} & \Delta L^{(p-1,p)} & 0 & & \\ & 0 & L^{(p,p-1)} & L^{(p)} & \Delta L^{(p,p+1)} & 0 & \\ & & 0 & \Delta L^{(p+1,p)} & L^{(p+1)} & \Delta L^{(p+1,p+2)} & \\ & & & & & & \ddots \end{pmatrix} \tag{B2}$$

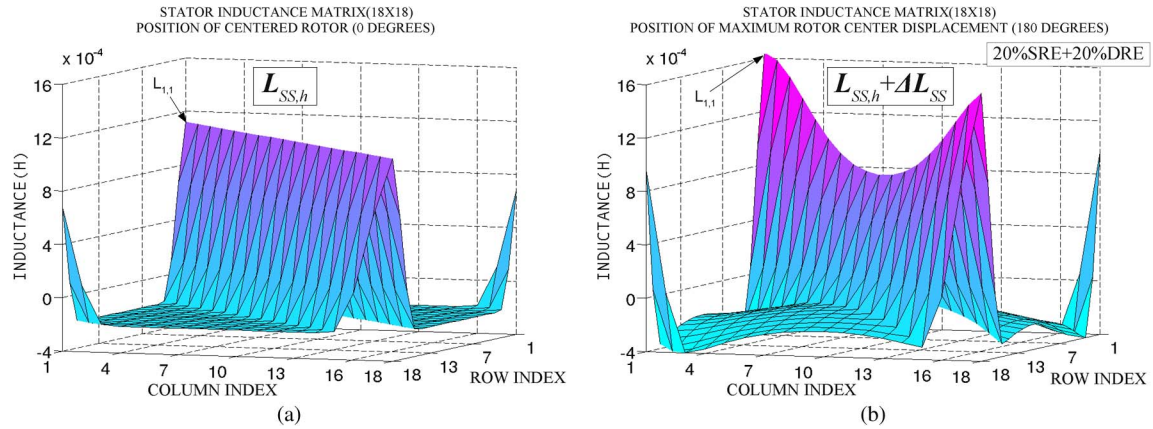

Fig. 15. $\boldsymbol{L}_{SS}$ matrix of a 1950-kVA six-pole RRSM with eccentricity (20% SRE + 20% DRE), displayed in two different instants during the rotor rotation. (a) Instantaneous position of centered rotor (when $\boldsymbol{L}_{SS} = \boldsymbol{L}_{SS,h}$). (b) After a rotation of 180°, when the rotor center is maximally displaced ($\boldsymbol{L}_{SS} = \boldsymbol{L}_{SS,h} + \Delta\boldsymbol{L}_{SS}$).

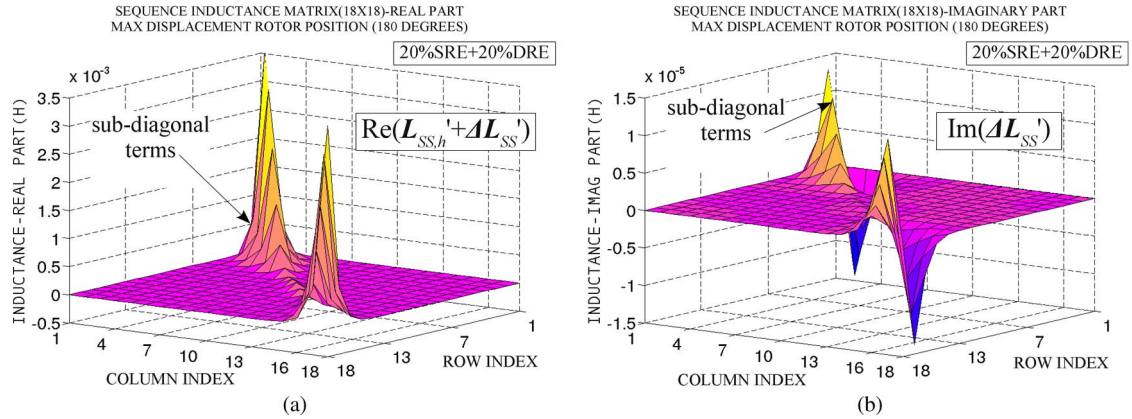

Fig. 16. Matrix in Fig. 15(b) is transformed by using (A4). (a) Real part of $\boldsymbol{L}'_{SS}$. (b) Imaginary part of $\boldsymbol{L}'_{SS}$ (note that $\mathrm{Im}(\boldsymbol{L}'_{SS}) = \mathrm{Im}(\boldsymbol{L}'_{SS,h} + \Delta\boldsymbol{L}'_{SS}) = \mathrm{Im}(\Delta\boldsymbol{L}'_{SS}) \approx \boldsymbol{0}$).

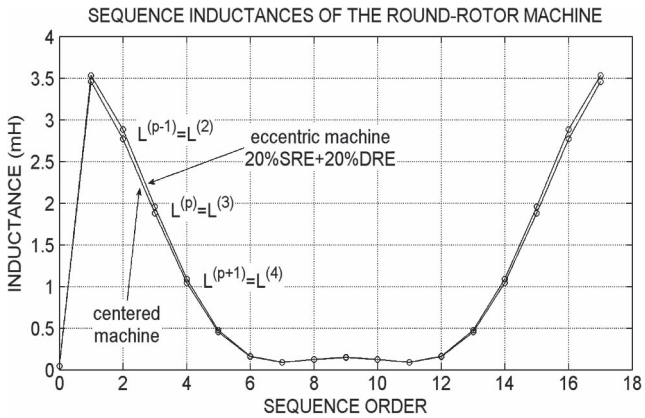

Fig. 17. Sequence inductances $L^{(q)}$ for the healthy and faulty 1950-kVA RRSM.

where $\Delta\boldsymbol{\psi}'_{SS} = \Delta\boldsymbol{L}'_{SS}\boldsymbol{i}'_S$ is posed for brevity. The column vector $\Delta\boldsymbol{\psi}'_{SS}$ has two terms of interest here, which are

$$\Delta\vec{\psi}_{SS}^{(p-1)} = \Delta L^{(p-1,p-2)}\vec{i}^{(p-2)} + \Delta L^{(p-1,p)}\vec{i}^{(p)} \quad \text{(B4)}$$

$$\Delta\vec{\psi}_{SS}^{(p+1)} = \Delta L^{(p+1,p)}\vec{i}^{(p)} + \Delta L^{(p+1,p+2)}\vec{i}^{(p+2)} \quad \text{(B5)}$$

and which appear in the sequence circuits of order $p \pm 1$ as follows:

$$\vec{v}^{(p\pm1)} = R_S\vec{i}^{(p\pm1)} + L^{(p\pm1)}\frac{d\vec{i}^{(p\pm1)}}{dt} + \frac{d}{dt}\Delta\vec{\psi}_{SS}^{(p\pm1)} + \vec{e}^{(p\pm1)}. \quad \text{(B6)}$$

Equation (B6) proves that the sequence circuit $p-1$ in Fig. 2 is coupled with the two contiguous circuits (of order $p-2$ and p). The same is true for the circuit $p+1$ (coupled with the circuits p and $p+2$). The coupling with $\vec{i}^{(p-2)}$ and $\vec{i}^{(p+2)}$ can be always neglected, due to the very low amplitudes of these currents (see the proofs in [35]). The coupling with the load current $\vec{i}^{(p)}$ is absent in no-load condition; thus, it was not considered in Fig. 2. However, this coupling is important in loaded conditions, as discussed in Section II-J.

Appendix C
Calculation of $K_{p\pm1}$ Coefficients

The integration constants $K_{p\pm1}$ in (14) and (19) are as follows:

$$K_{p\pm1} = \frac{p}{p\pm1}\sin\left(\frac{p\pm1}{p}\frac{\pi}{2}\right). \quad \text{(C1)}$$

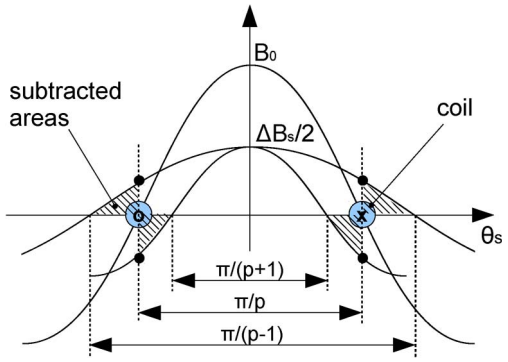

Fig. 18. Flux density wave integration.

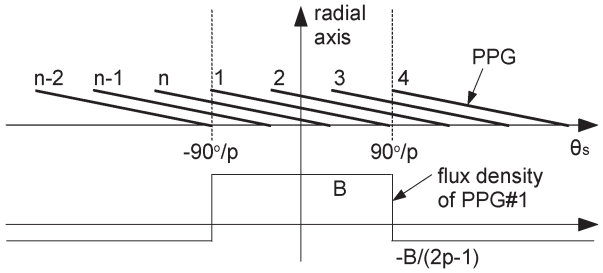

Fig. 19. Elementary winding with PPGs spanning 180 electrical degrees.

Equation (C1) is referred to an elementary coil spanning 180 electrical degrees (see Fig. 18). The flux linkages from the $2(p \pm 1)$-pole flux density waves differ from that of the fundamental due to some subtracted areas (the shaded areas in Fig. 18). The calculations can be perfected by taking into account winding distribution and step reduction, but more machine details should be known, with little gain of precision.

APPENDIX D
DEMONSTRATION OF (41)

Equation (41) is demonstrated by using (A5) and (C1), in the simplest case of an elementary winding made up of single-coil (concentrated) PPGs spanning 180 electrical degrees. The calculation can be always perfected by taking in account more winding details. Note that, from (C1), for $p \to \infty$, $K_{p\pm1} \to 1$, and (41) implies that $L^{(p)}$ is the mean value between $L^{(p-1)}$ and $L^{(p+1)}$, which can be directly verified in Fig. 17. In the general case for $p \geq 2$, the stator inductances (3) of an elementary winding, as shown in Fig. 19, can be carried out as

$$first\ row\ of\ \boldsymbol{L}_{SS}=\left(L_0\ \frac{L_0(4p-3)}{6p-3}\ \frac{L_0(2p-3)}{6p-3}\ \frac{-L_0}{2p-1}\ \dots\right). \tag{D1}$$

By using (D1) in (A5), the sequence inductances are carried out as ($a = 2L_0p/(6p-3)$ is posed for brevity)

$$L^{(q)} = \begin{cases} 0 & \text{for } q = 0 \\ a(3 + 4\cos q\delta + 2\cos 2q\delta) & \text{for } q \neq 0 \end{cases}. \tag{D2}$$

TABLE I
RATINGS FOR THE 1950-kVA GENERATOR

apparent power	1950kVA	power factor	0.80
line-line voltage/current	450V/2502A	frequency/speed	60Hz/1200rpm
unsaturated synchronous reactance			108mΩ
stator winding: 3-phase, symmetric, double-layer with 72 slots, 6 parallel PPGs per phase, 4 coils per PPG, 2 turns per coil, step reduction=5/6			

Since $p\delta = 60°$, from (D2) we have $L^{(p)} = 4a$. Finally, by using (C1) and (D2), we obtain

$$\left(L^{(p-1)}/K_{p-1} + L^{(p+1)}/K_{p+1}\right)/2 = a\frac{(3 + 2\cos\delta - \cos 2\delta) - \sqrt{3}(2\sin\delta + \sin 2\delta)/p}{\cos(90°/p)} \tag{D3}$$

whose limit for $p \to \infty$ is just $4a$. For $p = 2$, (D3) furnishes $3.7a$, which justifies (41) for any $p \geq 2$. The case for $p = 1$ requires a special study, which is not treated in this paper.

APPENDIX E

Table I reports rated data for the 1950-kVA machine.

REFERENCES

[1] G. Klempner and I. Kerszenbaum, "Handbook of large turbo-generator operation and maintenance," in *IEEE Power Engineering Series*. New York, NY, USA: Wiley, 2008.
[2] L. Romeral, J. C. Urresty, J. R. R. Ruiz, and A. G. Espinosa, "Modeling of surface-mounted permanent magnet synchronous motors with stator winding interturn faults," *IEEE Trans. Ind. Electron.*, vol. 58, no. 5, pp. 1576–1585, May 2011.
[3] A. Gandhi, T. Corrigan, and L. Parsa, "Recent advances in modeling and online detection of stator interturn faults in electrical motors," *IEEE Trans. Ind. Electron.*, vol. 58, no. 5, pp. 1564–1575, May 2011.
[4] S. Cheng, P. Zhang, and T. G. Habetler, "An impedance identification approach to sensitive detection and location of stator turn-to-turn faults in a closed-loop multiple-motor drive," *IEEE Trans. Ind. Electron.*, vol. 58, no. 5, pp. 1545–1554, May 2011.
[5] Z. Daneshi-Far, G. A. Capolino, and H. Henao, "Review of failures and condition monitoring in wind turbine generators," in *Proc. ICEM Conf.*, Rome, Italy, Sep. 6–8, 2010, pp. 1–6.
[6] D. Zarko, D. Ban, I. Vazdar, and V. Jaric, "Calculation of unbalanced magnetic pull in a salient-pole synchronous generator using finite-element method and measured shaft orbit," *IEEE Trans. Ind. Electron.*, vol. 59, no. 6, pp. 2536–2549, Jun. 2012.
[7] G. B. Pollock and J. F. Lyles, "Vertical hydraulic generators experience with dynamic air gap monitoring," *IEEE Trans. Energy Convers.*, vol. 7, no. 4, pp. 660–668, Dec. 1992.
[8] G. Traxler-Samek, R. Zickermann, and A. Schwery, "Cooling airflow, losses, and temperatures in large air-cooled synchronous machines," *IEEE Trans. Ind. Electron.*, vol. 57, no. 1, pp. 172–180, Jan. 2010.
[9] C. Bruzzese, "Field experience with the split-phase current signature analysis (SPCSA): Eccentricity assessment for a stand-alone alternator in time-varying and unbalanced load conditions," in *Proc. IEEE WEMDCD Conf.*, Paris, France, Mar. 11–12, 2013, pp. 257–270.
[10] D. Torregrossa, A. Khoobroo, and B. Fahimi, "Prediction of acoustic noise and torque pulsation in PM synchronous machines with static eccentricity and partial demagnetization using field reconstruction method," *IEEE Trans. Ind. Electron.*, vol. 59, no. 2, pp. 934–944, Feb. 2012.
[11] H. Henao, S. H. Kia, and G.-A. Capolino, "Torsional-vibration assessment and gear-fault diagnosis in railway traction system," *IEEE Trans. Ind. Electron.*, vol. 58, no. 5, pp. 1707–1717, May 2011.
[12] C. Bruzzese and T. Mazzuca, "DIEM project's outcomes: An automated air-gap monitoring approach for Italian Navy's on-board low-voltage generators," in *Proc. IEEE ESARS Conf.*, Bologna, Italy, Oct. 16–18, 2012, pp. 1–6.
[13] M. Delgado, G. Cirrincione, A. G. Espinosa, J. A. Ortega, and H. Henao, "Bearing faults detection by a novel condition monitoring scheme based

on statistical-time features and neural networks," *IEEE Trans. Ind. Electron.*, vol. 60, no. 8, pp. 3398–3407, Aug. 2013.
[14] C.-M. Vong, P.-K. Wong, and W.-F. Ip, "A new framework of simultaneous-fault diagnosis using pairwise probabilistic multi-label classification for time-dependent patterns," *IEEE Trans. Ind. Electron.*, vol. 60, no. 8, pp. 3372–3385, Aug. 2013.
[15] P. Talas and P. Toom, "Dynamic measurement and analysis of air gap variations in large hydroelectric generators," *IEEE Trans. PAS*, vol. PAS-102, no. 9, pp. 3098–3106, Sep. 1983.
[16] J. J. Simond, M. Tu Xuan, and R. Wetter, "An innovative inductive air-gap monitoring for large low speed hydro-generators," in *Proc. ICEM Conf.*, Vilamoura, Portugal, Sep. 6–9, 2008, pp. 1–5.
[17] C. Bruzzese, E. Santini, V. Benucci, and A. Millerani, "Model-based eccentricity diagnosis for a ship brushless generator exploiting the machine voltage signature analysis (MVSA)," in *Proc. IEEE SDEMPED Conf.*, Cargese, France, Aug. 31–Sep. 3, 2009, pp. 1–7.
[18] P. Zhang, Y. Du, T. G. Habetler, and B. Lu, "A survey of condition monitoring and protection methods for medium-voltage induction motors," *IEEE Trans. Ind. Appl.*, vol. 47, no. 1, pp. 34–46, Jan./Feb. 2011.
[19] S. Nandi, T. C. Ilamparithi, S. B. Lee, and D. Hyun, "Detection of eccentricity faults in induction machines based on nameplate parameters," *IEEE Trans. Ind. Electron.*, vol. 58, no. 5, pp. 1673–1683, May 2011.
[20] A. Bellini, F. Filippetti, C. Tassoni, and G.-A. Capolino, "Advances in diagnostic techniques for induction machines," *IEEE Trans. Ind. Electron.*, vol. 55, no. 12, pp. 4109–4126, Dec. 2008.
[21] C. Concari, G. Franceschini, and C. Tassoni, "Toward practical quantification of induction drive mixed eccentricity," *IEEE Trans. Ind. Appl.*, vol. 47, no. 3, pp. 1232–1239, May/Jun. 2011.
[22] D. Morinigo-Sotelo, L. A. Garcia-Escudero, O. Duque-Perez, and M. Perez-Alonso, "Practical aspects of mixed-eccentricity detection in PWM voltage-source-inverter-fed induction motors," *IEEE Trans. Ind. Electron.*, vol. 57, no. 1, pp. 252–262, Jan. 2010.
[23] J. Faiz and M. Ojaghi, "Instantaneous-power harmonics as indexes for mixed eccentricity fault in mains-fed and open/closed-loop drive-connected squirrel-cage induction motors," *IEEE Trans. Ind. Electron.*, vol. 56, no. 11, pp. 4718–4726, Nov. 2009.
[24] D. G. Dorrell, W. T. Thomson, and S. Roach, "Analysis of airgap flux, current, and vibration signals as a function of the combination of static and dynamic airgap eccentricity in 3-phase induction motors," *IEEE Trans. Ind. Appl.*, vol. 33, no. 1, pp. 24–34, Jan./Feb. 1997.
[25] S. Nandi, R. M. Bharadwaj, and H. A. Toliyat, "Performance analysis of a three-phase induction motor under incipient mixed eccentricity condition," *IEEE Trans. Energy Convers.*, vol. 17, no. 3, pp. 392–399, Sep. 2002.
[26] J. R. Fatemi, H. Henao, G.-A. Capolino, and S. Sieg-Zieba, "Load influence on induction machine torque and stator current in case of shaft misalignment," in *Proc. IEEE IECON Conf.*, Porto, Portugal, Nov. 3–5, 2009, pp. 3449–3454.
[27] A. Ceban, R. Pusca, and R. Romary, "Study of rotor faults in induction motors using external magnetic field analysis," *IEEE Trans. Ind. Electron.*, vol. 59, no. 5, pp. 2082–2093, May 2012.
[28] A. Tessarolo, C. Bassi, and D. Giulivo, "Time-stepping finite-element analysis of a 14-MVA salient-pole shipboard alternator for different damper winding design solutions," *IEEE Trans. Ind. Electron.*, vol. 59, no. 6, pp. 2524–2535, Jun. 2012.
[29] T. C. Ilamparithi and S. Nandi, "Detection of eccentricity faults in three-phase reluctance synchronous motor," *IEEE Trans. Ind. Appl.*, vol. 48, no. 4, pp. 1307–1317, Jul./Aug. 2012.
[30] C. Bruzzese, A. Giordani, and E. Santini, "Static and dynamic rotor eccentricity on-line detection and discrimination in synchronous generators by no-load E.M.F. space vector analysis," in *Proc. SPEEDAM Conf.*, Ischia, Italy, Jun. 18–20, 2008, pp. 1259–1264.
[31] C. Bruzzese and G. Joksimovic, "Harmonic signatures of static eccentricities in the stator voltages and in the rotor current of no-load salient pole synchronous generators," *IEEE Trans. Ind. Electron.*, vol. 58, no. 5, pp. 1606–1624, May 2011.
[32] P. Neti and S. Nandi, "Stator interturn fault detection of synchronous machines using field current and rotor search-coil voltage signature analysis," *IEEE Trans. Ind. Appl.*, vol. 45, no. 3, pp. 911–920, May/Jun. 2009.
[33] M. Biet, "Rotor faults diagnosis using features selection and nearest neighbors rule: Application to a turbogenerator," *IEEE Trans. Ind. Electron.*, vol. 60, no. 9, pp. 4063–4073, Sep. 2013.
[34] C. Bruzzese, "Diagnosis of eccentric rotor in synchronous machines by analysis of split-phase currents—Part II: Experimental analysis," *IEEE Trans. Ind. Electron.*, IEEE Xplore Early Access, Oct. 1, 2013. DOI: 10.1109/TIE.2013.2284554.
[35] C. Bruzzese, "Study of cardioid-shaped loop current space vector trajectories for rotor eccentricity detection in power synchronous machines," in *Proc. IEEE SDEMPED Conf.*, Bologna, Italy, Sep. 5–8, 2011, pp. 205–212.
[36] C. Bruzzese, "A virtual instrument for on-line evaluation of alternator's shaft misalignments through ICSVA (internal current space-vector analysis)," in *Proc. IEEE SDEMPED Conf.*, Bologna, Italy, Sep. 5–8, 2011, pp. 55–62.
[37] C. Bruzzese, "Analysis and application of particular current signatures (symptoms) for cage monitoring in non-sinusoidally fed motors with high rejection to drive load, inertia, and frequency variations," *IEEE Trans. Ind. Electron.*, vol. 55, no. 12, pp. 4137–4155, Dec. 2008.
[38] H. Henao, G. A. Capolino, T. Assaf, M. F. Cabanas, M. G. Melero, G. A. Orcajo, J. M. Cano, and F. Briz del Blanco, "A new mathematical procedure for the computation of the equivalent inverse sequence impedance in working induction motors," in *Proc. IEEE Ind. Appl. Conf.*, Rome, Italy, Oct. 8–12, 2000, pp. 336–343.
[39] H. Henao, C. Martis, and G.-A. Capolino, "An equivalent internal circuit of the induction machine for advanced spectral analysis," *IEEE Trans. Ind. Appl.*, vol. 40, no. 3, pp. 726–734, May/Jun. 2004.
[40] M. J. DeBortoli, S. J. Salon, D. W. Burow, and C. J. Slavik, "Effects of rotor eccentricity and parallel windings on induction machine behavior: A study using finite element analysis," *IEEE Trans. Magn.*, vol. 29, no. 2, pp. 1676–1682, Mar. 1993.
[41] C. Bruzzese, O. Honorati, and E. Santini, "Evaluation of classic and innovative sideband-based broken bar indicators by using an experimental cage and a transformed (n,m) complex model," in *Proc. IEEE ISIE Conf.*, Vigo, Spain, Jun. 4–7, 2007, pp. 1264–1269.
[42] R. Perers, U. Lundin, and M. Leijon, "Saturation effects on unbalanced magnetic pull in a hydroelectric generator with an eccentric rotor," *IEEE Trans. Magn.*, vol. 43, no. 10, pp. 3884–3890, Oct. 2007.
[43] S. M. A. Cruz and A. J. M. Cardoso, "Stator winding fault diagnosis in three-phase synchronous and asynchronous motors, by the extended Park's vector approach," *IEEE Trans. Ind. Appl.*, vol. 37, no. 5, pp. 1227–1233, Sep./Oct. 2001.

Claudio Bruzzese (S'05–M'08) received the M.Sc. (*cum laude*) and Ph.D. degrees from the University of Rome "La Sapienza," Rome, Italy, in 2002 and 2008, respectively.

After graduation, he was with the National Power System Management Company. He was a Visiting Researcher with the University of Victoria, Victoria, Canada, in 2012. Since September 2002, he has been an Assistant Researcher with the Department of Astronautical, Electrical, and Energy Engineering, University of Rome "La Sapienza," where he has been an Assistant Professor since 2011. He is a Consultant for the Italian Ministry of Defense and has developed research projects for the Military Research National Program. He has authored or coauthored about 60 technical papers, and holds four patents. His research interests cover fault diagnosis of power induction and synchronous machines, railway and naval power systems, linear drives, and electromechanical design and advanced modeling.

Dr. Bruzzese is member of the IEEE Industrial Electronics Society. He is also a Registered Professional Engineer in Italy.